

A Model of Diffuse Galactic Radio Emission from 10 MHz to 100 GHz

Angélica de Oliveira-Costa¹, Max Tegmark¹, B.M. Gaensler², Justin Jonas³, T.L. Landecker⁴, Patricia Reich⁵

¹MIT Kavli Institute & Dept. of Physics, Massachusetts Institute of Technology, Cambridge, MA 02139, USA

²School of Physics A29, The University of Sydney, NSW 2006, Australia

³Department of Physics & Electronics, Rhodes University, Grahamstown 6140, South Africa

⁴Dominion Radio Astrophysical Observatory, National Research Council, P.O. Box 248, Penicton, B.C., Canada

⁵Max-Planck-Institut für Radioastronomie, Auf dem Hügel 69, D-53121 Bonn, Germany

Accepted —; Received —; in original form —.

ABSTRACT

Understanding diffuse Galactic radio emission is interesting both in its own right and for minimizing foreground contamination of cosmological measurements. Cosmic Microwave Background experiments have focused on frequencies $\gtrsim 10$ GHz, whereas 21 cm tomography of the high redshift universe will mainly focus on $\lesssim 0.2$ GHz, for which less is currently known about Galactic emission. Motivated by this, we present a global sky model derived from all publicly available total power large-area radio surveys, digitized with optical character recognition when necessary and compiled into a uniform format, as well as the new Villa Elisa data extending the 1.42 GHz map to the entire sky. We quantify statistical and systematic uncertainties in these surveys by comparing them with various global multi-frequency model fits. We find that a principal component based model with only three components can fit the 11 most accurate data sets (at 10, 22, 45 & 408 MHz and 1.42, 2.326, 23, 33, 41, 61, 94 GHz) to an accuracy around 1%-10% depending on frequency and sky region. Both our data compilation and our software returning a predicted all-sky map at any frequency from 10 MHz to 100 GHz are publicly available at <http://space.mit.edu/home/angelica/gsm>.

Key words: cosmology: diffuse radiation – methods: data analysis

1 INTRODUCTION

There has been a great deal of interest in mapping diffuse Galactic radio emission, both to better understand our Galaxy and to clean out foreground contamination from Cosmic Microwave Background (CMB) maps. For reviews of such issues, see, *e.g.*, from (1) to (23), and references therein. Because much of this work was both motivated by the CMB and based on maps from CMB experiments, it has focused primarily on frequencies above 10 GHz. Now that Neutral Hydrogen Tomography (NHT) is emerging as a promising cosmological tool where we can map the high-redshift universe three-dimensionally via the redshifted 21 cm line – see, *e.g.*, from (24) to (44) – it is timely to extend these efforts down to lower frequencies. The redshift range $7 \gtrsim z \gtrsim 50$ where NHT may be feasible corresponds to the frequency range 30 – 180 MHz. Indeed, accurate foreground modeling is arguably even more important for NHT than for CMB: whereas unpolarized CMB fluctuations dominate over foregrounds for the most favorable frequencies and sky directions, and the situation for polarized CMB fluctuations is only 1-2 orders of magnitude worse, the cosmological neutral hy-

drogen signal is perhaps four orders of magnitudes smaller than the relevant foregrounds – see, *e.g.*, from (45) to (49).

In due time, NHT experiments such as LOFAR (35; 36; 37), MWA (45; 47) and 21CMA (40) will produce accurate low-frequency maps of Galactic emission much like CMB experiments have above 10 GHz. Even now, however, it is important to have a model for how this emission varies across the sky and across the NHT-relevant frequency band, because this helps optimize experimental design, scan strategy and data analysis pipelines to maximize the scientific return on its investment. Even as new maps are made of small patches of sky, it is valuable to have a pre-existing global sky model to be able to quantify and mitigate contamination from distant sidelobes.

As described in Section 2, the radio astronomy community has produced a large number of sky surveys over the years, many of which are directly relevant to the NHT frequency range. However, most of them have never been used by cosmology community, because of various challenges: many are not publicly available in electronic form, and they are also hard to combine because they differ in sky coverage, angular resolution, pixelization and quality. Instead, a common approach among cosmologists has been to sim-

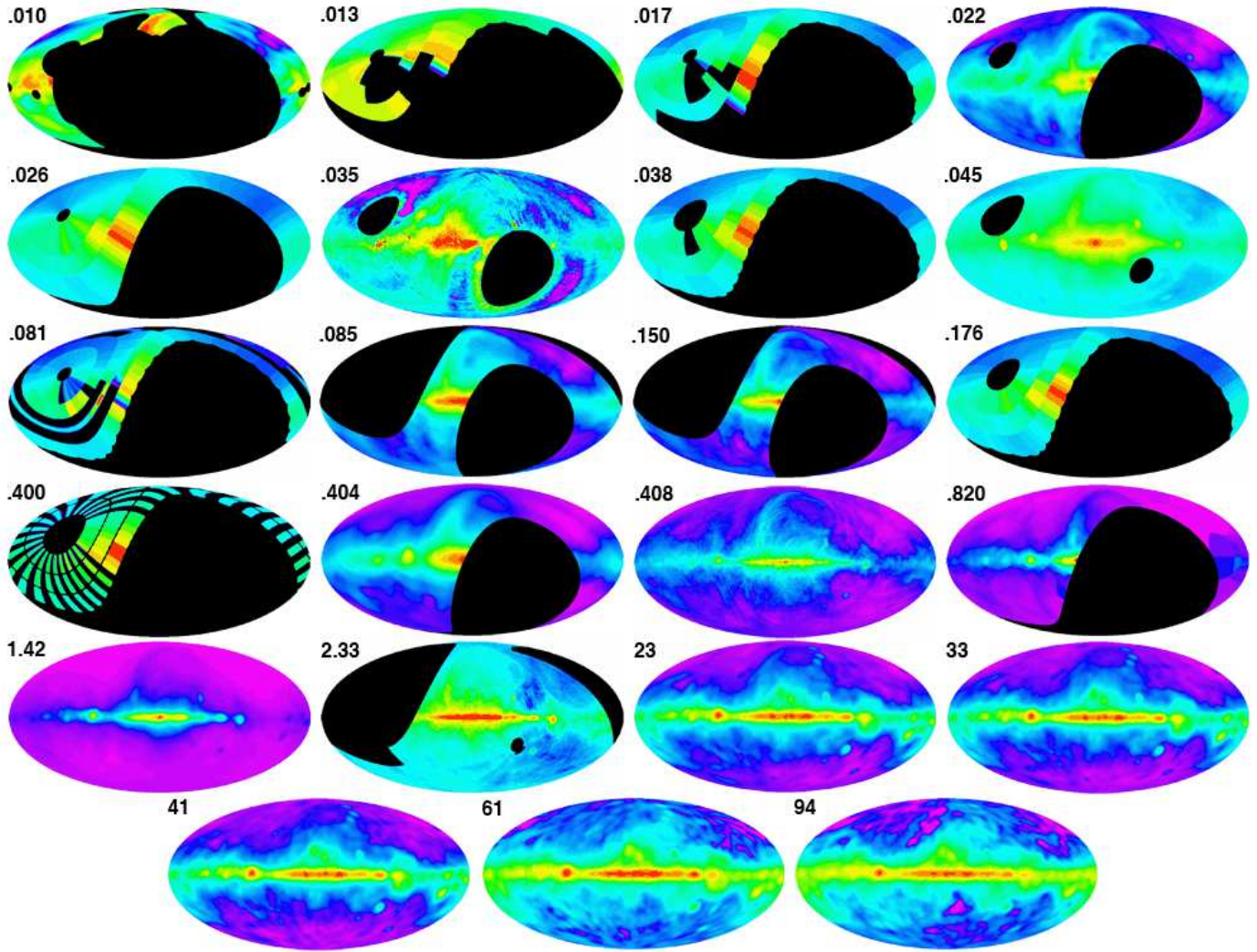


Figure 1. The maps show (from left to right, top to bottom) the 0.010 GHz (52), 0.0135 GHz (55), 0.0175 GHz (55), 0.022 GHz (57), 0.026 GHz (58), 0.0345 GHz (61), 0.038 GHz (58), 0.045 GHz (63), 0.0815 GHz (55), 0.085 GHz (65), 0.150 GHz (65), 0.176 GHz (58), 0.400 GHz (58), 0.404 GHz (72), 0.408 GHz (50), 0.820 GHz (73), 1.42 GHz (74; 75; 76) and 2.326 GHz (78) surveys, and the CMB-free WMAP foreground maps at 23, 33, 41, 61 and 94 GHz (18; 19; 22; 79).

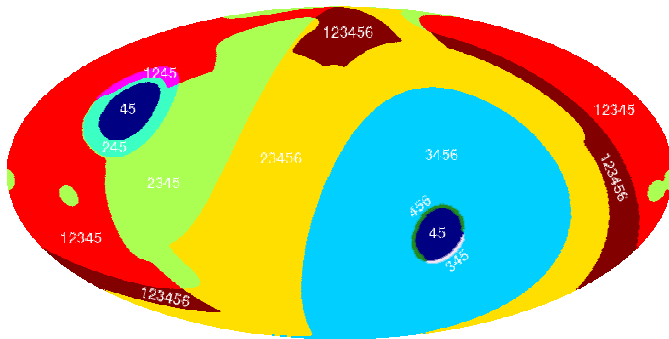


Figure 2. Sky coverage/overlap, in Galactic coordinates, of the six key maps below the WMAP frequencies: the numbers from 1 to 6 correspond to 10, 22, 45, 408, 1420 and 2326 MHz, respectively.

ply extrapolate the 408 MHz Haslam map (50) to lower frequencies, thus ignoring any spectral variation across the sky. As we will see, significantly better accuracy can be attained by modeling that

includes additional data sets. The goal of the present paper is to collect, standardize and model this large body of radio data to make it more useful to the cosmology community.

The rest of this paper is organized as follows. In Section 2, we describe how we compile all publicly available total power large-area radio surveys of which we are aware, digitizing them with optical character recognition when necessary, and converting them into a uniform format. In Section 3, we compare different methods for constructing a global sky model from this data that covers the entire sky and the entire frequency range. In Section 4, we present the results of our modeling, quantify the accuracy of our best model, and briefly comment on implications for the physics underlying this emission.

2 DATA SETS

In order to carry out our analysis, we performed a literature search for large-area total power sky surveys in the frequency range 1 MHz to 100 GHz. The result of our search is shown in Figure 1

Table 1. Available total power radio surveys.

Ref	ν [GHz]	FWHM [$^{\circ}$]	Region		Observatory	Status
			RA	DEC		
(51)	0.00393	60	$00^{\text{h}} < \alpha < 24^{\text{h}}$	$-60^{\circ} < \delta < +60^{\circ}$	RAE-1	D
(51)	0.00655	60	$00^{\text{h}} < \alpha < 24^{\text{h}}$	$-60^{\circ} < \delta < +60^{\circ}$	RAE-1	D
(52)	0.010	2.6x1.9	$00^{\text{h}} < \alpha < 16^{\text{h}}$	$-06^{\circ} < \delta < +74^{\circ}$	DRAO, CAN	A
(53)	0.010	5	$00^{\text{h}} < \alpha < 24^{\text{h}}$	$-65^{\circ} < \delta < +90^{\circ}$	DRAO(CAN),AUS	D
(54)	0.0102	4x5	$00^{\text{h}} < \alpha < 24^{\text{h}}$	$-65^{\circ} < \delta < -02^{\circ}$	AUS	D
(55)	0.0135	53x12	$00^{\text{h}} < \alpha < 24^{\text{h}}$	$(16,35,52,69)^{\circ}$	ENG	C
(56)	0.0165	1.5	$00^{\text{h}} < \alpha < 24^{\text{h}}$	$-90^{\circ} < \delta < 00^{\circ}$	Tasmania, AUS	D
(55)	0.0175	12x17	$00^{\text{h}} < \alpha < 24^{\text{h}}$	$(16,35,52,69)^{\circ}$	ENG	C
(57)	0.022	1.1x1.7	$00^{\text{h}} < \alpha < 24^{\text{h}}$	$-28^{\circ} < \delta < +80^{\circ}$	DRAO, CAN	A
(58)	0.026	15x44	$00^{\text{h}} < \alpha < 24^{\text{h}}$	$(20,40,60)^{\circ}$	ENG	C
(59)	0.030	11	$00^{\text{h}} < \alpha < 24^{\text{h}}$	$-90^{\circ} < \delta < 00^{\circ}$	Parkes, AUS	D
(60)	0.030	11	$00^{\text{h}} < \alpha < 24^{\text{h}}$	$-90^{\circ} < \delta < +90^{\circ}$		D
(61)	0.0345	0.4x0.7	$00^{\text{h}} < \alpha < 24^{\text{h}}$	$-30^{\circ} < \delta < +60^{\circ}$	GEETEE, IND	A
(62)	0.038	7.5	$00^{\text{h}} < \alpha < 24^{\text{h}}$	$-25^{\circ} < \delta < +70^{\circ}$	Jodrell Bank, ENG	D
(58)	0.038	15x44	$00^{\text{h}} < \alpha < 24^{\text{h}}$	$(20,40,60)^{\circ}$	ENG	C
(63)	0.045	4.6x2.4	$00^{\text{h}} < \alpha < 24^{\text{h}}$	$-90^{\circ} < \delta < +19^{\circ}$	CHL	B
(64)	0.045	3.6x3.6	$00^{\text{h}} < \alpha < 24^{\text{h}}$	$+05^{\circ} < \delta < +65^{\circ}$	JPN	B
(55)	0.0815	12x17	$00^{\text{h}} < \alpha < 24^{\text{h}}$	$(16,25,30,35,40,52,69)^{\circ}$	ENG	C
(65)	0.085	3.8x3.5	$00^{\text{h}} < \alpha < 24^{\text{h}}$	$-25^{\circ} < \delta < +25^{\circ}$	Parkes, AUS	C,A
(66)	0.100	17	$00^{\text{h}} < \alpha < 24^{\text{h}}$	$-90^{\circ} < \delta < +30^{\circ}$	AUS	D
(65)	0.150	2.2x2.2	$00^{\text{h}} < \alpha < 24^{\text{h}}$	$-25^{\circ} < \delta < +25^{\circ}$	Parkes, AUS	C,A
(67)	0.153	2.2	$00^{\text{h}} < \alpha < 24^{\text{h}}$	$-90^{\circ} < \delta < +05^{\circ}$	Parkes, AUS	D
(68)	0.160	8x6	$16^{\text{h}} < \alpha < 22^{\text{h}}$	$-33^{\circ} < \delta < +90^{\circ}$	Wheaton, USA	D
(58)	0.176	15x44	$00^{\text{h}} < \alpha < 24^{\text{h}}$	$(20,40,60)^{\circ}$	ENG	C
(69)	0.178	0.2x4.6	$00^{\text{h}} < \alpha < 24^{\text{h}}$	$-05^{\circ} < \delta < +90^{\circ}$	ENG	D
(70)	0.200		$00^{\text{h}} < \alpha < 24^{\text{h}}$	$-90^{\circ} < \delta < +45^{\circ}$	Commonwealth, AUS	D
(71)	0.200	16.8	$00^{\text{h}} < \alpha < 24^{\text{h}}$	$-20^{\circ} < \delta < +90^{\circ}$	Kieler, GER	D
(58)	0.400	8.5x6.5	$00^{\text{h}} < \alpha < 24^{\text{h}}$	$(20,40,60)^{\circ}$	ENG	C
(72)	0.404	7.5	$00^{\text{h}} < \alpha < 24^{\text{h}}$	$-20^{\circ} < \delta < +90^{\circ}$	ENG	C
(50)	0.408	0.8	$00^{\text{h}} < \alpha < 24^{\text{h}}$	$-90^{\circ} < \delta < +90^{\circ}$	GER, AUS, ENG	A
(73)	0.820	1.2	$00^{\text{h}} < \alpha < 24^{\text{h}}$	$-07^{\circ} < \delta < +85^{\circ}$	Dwingeloo, NLD	C,A
(74; 75)	1.42	0.6	$00^{\text{h}} < \alpha < 24^{\text{h}}$	$-19^{\circ} < \delta < +90^{\circ}$	Stockert, GER	A
(76)	1.42	0.6	$00^{\text{h}} < \alpha < 24^{\text{h}}$	$-90^{\circ} < \delta < -10^{\circ}$	Villa Elisa, ARG	B
(77)	2.3	2.3x1.9	$00^{\text{h}} < \alpha < 24^{\text{h}}$	$-53^{\circ} < \delta < +35^{\circ}$	BRA	D
(78)	2.326	0.3	$00^{\text{h}} < \alpha < 24^{\text{h}}$	$-83^{\circ} < \delta < +32^{\circ}$	Hartebeesthoek, ZAF	B
(80; 81)	19	3	$00^{\text{h}} < \alpha < 24^{\text{h}}$	$-15^{\circ} < \delta < +75^{\circ}$	Ballou, USA	B
(18; 19; 22; 79)	23	0.88	$00^{\text{h}} < \alpha < 24^{\text{h}}$	$-90^{\circ} < \delta < +90^{\circ}$	WMAP	A
(82)	31	7	$00^{\text{h}} < \alpha < 24^{\text{h}}$	$-90^{\circ} < \delta < +90^{\circ}$	COBE/DMR	A
(18; 19; 22; 79)	33	0.66	$00^{\text{h}} < \alpha < 24^{\text{h}}$	$-90^{\circ} < \delta < +90^{\circ}$	WMAP	A
(18; 19; 22; 79)	41	0.51	$00^{\text{h}} < \alpha < 24^{\text{h}}$	$-90^{\circ} < \delta < +90^{\circ}$	WMAP	A
(82)	53	7	$00^{\text{h}} < \alpha < 24^{\text{h}}$	$-90^{\circ} < \delta < +90^{\circ}$	COBE/DMR	A
(18; 19; 22; 79)	61	0.35	$00^{\text{h}} < \alpha < 24^{\text{h}}$	$-90^{\circ} < \delta < +90^{\circ}$	WMAP	A
(82)	90	7	$00^{\text{h}} < \alpha < 24^{\text{h}}$	$-90^{\circ} < \delta < +90^{\circ}$	COBE/DMR	A
(18; 19; 22; 79)	94	0.22	$00^{\text{h}} < \alpha < 24^{\text{h}}$	$-90^{\circ} < \delta < +90^{\circ}$	WMAP	A

A = Publicly available in digital form.

B = Available on request.

C = Available as printed table (which we OCR'd).

D = Not available in any numerical form.

and Table 1. Unfortunately, some of the surveys shown in Table 1 are not available in any numerical form. A minority of the surveys are publicly available in digital form (and/or) available on request, while many of the surveys are available only as printed tables which we converted to digital form using Optical Character Recognition (OCR).

Some of the surveys shown in Figure 1 have a very large angular beam (the 0.0135, 0.0175, 0.026, 0.038, 0.0815, 0.176, 0.400 and the 0.404 GHz maps), others are undersampled (the 0.085 and

the 0.150 surveys), the 0.820 GHz survey is smoothed to 5° in its anti-centre area and, finally, one of them, the 0.0345 GHz map, it is missing large-scale structures and has severe striping that makes it unsuitable for use in our analysis. Therefore, all analysis presented in this paper is performed using the 0.010, 0.022, 0.045, 0.408, 1.42, 2.326, 23, 33, 41, 61 and the 94 GHz maps – Figure 2 shows the sky coverage of these different surveys and how they overlap. They were all transformed to Galactic coordinates, pixelized using the HealPix RING scheme (83) with resolution $n_{\text{side}}=512$ (which

corresponds to $12 \times 512^2 = 3,145,728$ equal-area pixels across the sky), and had the CMB component of 2.725 K subtracted. For the five 5-year WMAP maps (84) used in this analysis, we removed their CMB component as described in (18; 22)¹ and then converted these maps to antenna temperature. Before performing our main analysis, we smooth all maps to a common final angular resolution of 5.1° . However, as described below, we also use full-resolution maps for some other purposes.

3 METHODS

A wide variety of models of Galactic emission have been used in the literature – see, *e.g.*, (1; 3; 7; 8; 14) and references therein, and there are many additional popular fitting techniques that are purely statistical in nature and do not assume anything about the underlying physics. To maximize the utility of the available data sets and all the hard work that observers have invested into obtaining them, we explored a wide range of modeling methods before selecting one. Below we first present the criterion we will use for choosing the best modeling technique, then explore a range of methods to select the one that is most useful for our goal. The models we compare include physics-inspired fitting functions, power laws, polynomials and splines as well as principal components.

3.1 Criteria: accuracy and simplicity

In this paper, our main criterion for choosing a method is accuracy. In other words, we wish to find the method that most accurately predicts the Galactic emission in any arbitrary sky direction and at any frequency between 0.010 to 94 GHz, independently of whether it is based on physical assumptions or is “blind” and purely statistical. In practice, we implement this criterion as follows: for each of the 11 frequencies where a high-quality sky map is available, we quantify how accurately a method can predict this map by using only information from the other 10 maps.

Since the map used as the “truth” in each test may itself have noise and systematic errors, this procedure can overestimate the true errors. Moreover, our final Global Sky Model (GSM) uses all 11 input maps jointly, not merely 10 at a time, and it is therefore more accurate than the model used in the test. For both of these reasons, the accuracy numbers we quote later on should be interpreted as conservative worst-case bounds on the actual accuracy.

In addition to accuracy, we also desire simplicity. Specifically, it is valuable if the modeling method is simple and transparent enough to allow an analytical understanding of how the input determines the output, especially if this makes it possible to characterize how noise and systematic errors propagate and affect the statistical properties of the resulting model.

3.2 Method comparison

3.2.1 Single-component models

The Galactic InterStellar Medium (ISM) is a highly complex medium with many different constituents interacting through a multitude of physical processes. Free electrons spiraling around the Galactic magnetic field lines emit synchrotron radiation (85). For

¹ The new foreground-cleaned 5 year WMAP map and the five foreground-only maps are available on the web site <http://space.mit.edu/home/angelica/gsm> (bottom of page).

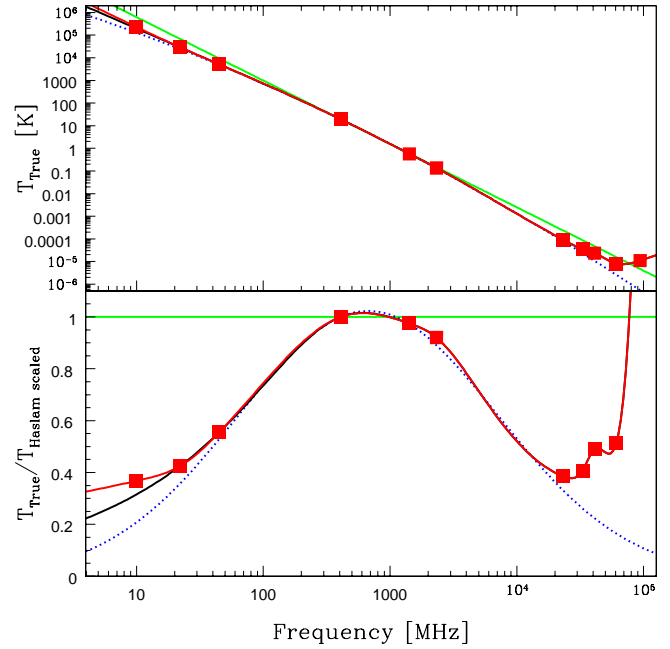


Figure 3. Comparison between the different GSM methods presented in Section 3.2. Squares show the 11 measurements available at a pixel at $(l, b) = (11.3^\circ, 89.6^\circ)$. Lines show fits based on power-law-scaling of the Haslam map (straight solid/green line), a quadratic polynomial in log-log (dotted/blue curve), a cubic spline without the leftmost point (straight solid/black), and a 3-component PCA fit (straight solid/red). In the lower panel, the curves have been divided by the power-law-scaling of the Haslam map to make discrepancies between the methods even more visible.

the lower frequencies where synchrotron radiation is expected to dominate the Galactic emission, a common approach in the literature has been to simply scale the Haslam map (50) in frequency, usually with a power law

$$T(\hat{\mathbf{r}}_i, \nu) = T(\hat{\mathbf{r}}_i, \nu_*) \left(\frac{\nu}{\nu_*} \right)^\beta, \quad (1)$$

where $\hat{\mathbf{r}}_i$ is the unit vector pointing toward the i^{th} pixel in the map, ν is the frequency which this map is being scaled to, $\nu_* = 408$ MHz is the Haslam frequency, β is the spectral index², and T is the brightness temperature. However, the frequency dependence is known not to be a perfect power law: at higher frequencies, the slope of the synchrotron spectrum typically steepens³, and other Galactic components such as free-free and dust emission begin to dominate. This suggests the use of a more general scaling of the type

$$T(\hat{\mathbf{r}}_i, \nu) = T(\hat{\mathbf{r}}_i, \nu_*) f(\nu_i), \quad (2)$$

where the spectrum $f(\nu_i)$ is optimized by fitting to maps at other frequencies. We will quantify the accuracy of this approach in Section 4. The main problem with it is that the foreground frequency

² The straight green line in the upper panel of Figure 3 shows the case $\beta = -2.8$.

³ One expects a spectral steepening towards higher frequencies, corresponding to a softer electron spectrum ((86); Fig 5.3 in (87)). A recent analysis done at 22 MHz (57) shows that β varies slightly over a large frequency range (88; 89; 90; 91).

dependence is known to vary across the sky. This occurs both because the synchrotron spectral index β depends on the energy distribution of relativistic electrons (85), which varies somewhat across the sky, and also because the ratio of synchrotron to dust and other emission components can vary from place to place. In contrast, equation (2) assumes that a map of Galactic emission looks the same at all frequencies except for an overall change in amplitude.

3.2.2 Polynomial and spline fitting

Now that so much data is available, it is tempting to allow much more general fitting functions such as polynomials or cubic splines. We tested both of these approaches here and found that they gave their most accurate results when fitting in log-log (when fitting $\lg T$ as a function of $\lg \nu$ rather than using T and/or ν directly), since the function to be fit is then rather smooth – see Figure 3 (top panel). For instance, the quadratic polynomial fit

$$\ln T(\hat{\mathbf{r}}_i, \nu) = \alpha(\hat{\mathbf{r}}_i) + \beta(\hat{\mathbf{r}}) \ln \frac{\nu}{\nu_*} + \gamma(\hat{\mathbf{r}}_i) \left(\ln \frac{\nu}{\nu_*} \right)^2 \quad (3)$$

generalizes equation (1) to a position-dependent “running” γ of the spectral index β . For a given pixel i , let m_i denote the number of surveys that have observed it ($6 \leq m_i \leq 11$). Re-writing equation (3) in a matrix form, we obtain

$$\mathbf{y} = \mathbf{A}\mathbf{x} + \mathbf{n}, \quad (4)$$

where \mathbf{y} is an m_i -dimensional vector that contains (the logarithm of) the temperatures at the i^{th} pixel at the m_i survey frequencies, \mathbf{A} is an $m_i \times 3$ matrix that encodes the frequency dependence, and \mathbf{x} is a 3-dimensional vector that contains the α , β and γ values at the i^{th} pixel. The extra term \mathbf{n} denotes noise in the broadest sense of the word, *i.e.*, receiver noise, uncorrected offsets and calibration errors, and any other systematic effects or other non-sky signals present in the survey maps. This is an overdetermined system of linear equations since we always have $m_i > 3$ input maps available, and assuming that the noise has zero mean, *i.e.*, $\langle \mathbf{n} \rangle = \mathbf{0}$, the minimum-variance estimator for \mathbf{x} is

$$\hat{\mathbf{x}} = [\mathbf{A}^t \mathbf{N}^{-1} \mathbf{A}]^{-1} \mathbf{A}^t \mathbf{N}^{-1} \mathbf{y}, \quad (5)$$

with covariance matrix

$$\Sigma = [\mathbf{A}^t \mathbf{N}^{-1} \mathbf{A}]^{-1}, \quad (6)$$

where \mathbf{N} is the noise covariance matrix $\langle \mathbf{n}\mathbf{n}^t \rangle$. In Figure 3, we have simply approximated \mathbf{N} by the diagonal matrix with N_{ii} given by the *rms* of the i^{th} map (we find the recovered maps to be rather insensitive to the choice of \mathbf{N}). By performing this calculation for all the pixels in the sky, we obtain all-sky maps of the quantities α , β and γ . Finally, to obtain a sky map at any frequency ν , we simply use these values of α , β and γ in equation (3).

We also tried the approach of fitting the (log-log) frequency dependence in each pixel to a separate cubic spline. This involves even more fitting parameters (between 6 and 11), as the resulting curve is forced to match the data exactly at all observed frequencies. Maps of α , β and γ can then be produced by computing the first and second derivatives of the spline function.

Figure 3 illustrates the pros and cons of the above-mentioned methods. Both the simple power law and the log-log quadratic polynomial are seen to provide poor fits simply because the physics is more complex than these functions can model. The figure shows that a power law is a poor approximation even in the synchrotron-dominated regime $\nu \gtrsim 1$ GHz, because of a distinct steepening of the spectrum towards higher frequencies. However, the figure

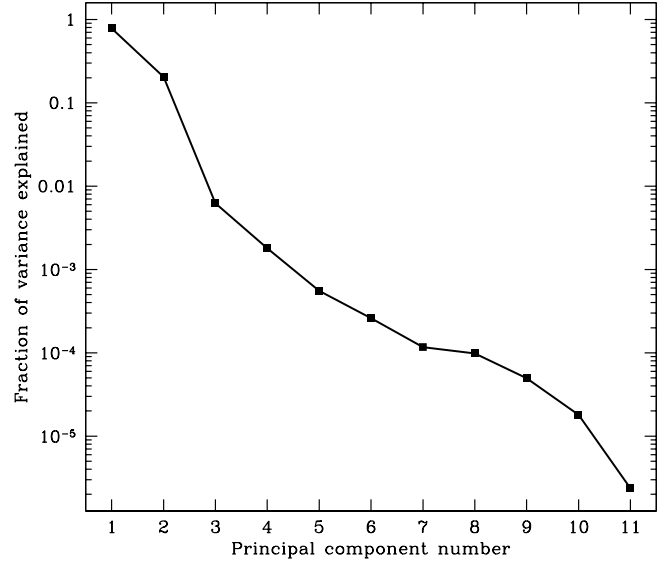


Figure 4. The eigenvalues $\lambda_i/11$ for the 11 principal components, which can be interpreted as the fraction of the total variance at the 11 frequencies that each component explains.

shows that going to the opposite extreme and allowing too many fitting parameters causes problems as well, from overfitting the data. The spline blindly goes through all the data points without any regard for what constitutes physically reasonable behavior, and sure enough is seen to perform poorly when forced to extrapolate. The ability to extrapolate reliably is crucial to our sky model because many of our input maps have only partial sky coverage. A related drawback of the spline approach is that if one of the input maps has more noise or systematic errors than others, this will fully propagate into the model rather than getting “voted down” by the other input maps.

A final problem, seen most clearly in the bottom panel, is caused by fitting the log of the temperature rather than the temperature itself: a relatively modest error in the predicted log-temperature translates into an exponentially amplified error in the temperature itself. The logarithmic fitting also complicates the modeling of measurement errors: if they are symmetrically distributed around zero and uncorrelated with the sky signal in the raw input maps, this is no longer true for the log-maps. In contrast, a linear combination of the linear input maps would preserve such desirable statistical properties of the noise.

3.2.3 Principal Component Analysis

The above examples suggest that we should try a method that: (1) can fit the spectral behavior of the data with as few parameters as possible; and (2) is linear (takes some linear combination of the raw input maps). In other words, we want a linear fitting method where the data itself is allowed to select the optimal parametrized form for the frequency dependence. Fortunately, the standard tool known as Principal Component Analysis (PCA) does exactly this (92). Indeed, we find that PCA performs better than all the approaches tried above when we implement it as described below.

Table 2. The three first principal components.

ν [GHz]	rms		Comp1	Comp2	Comp3
0.010	262344 K		0.286	-0.358	-0.121
0.022	33693 K		0.304	-0.297	0.086
0.045	6506 K		0.306	-0.291	0.010
0.408	25.4 K		0.315	-0.251	0.020
1.420	0.862 K		0.314	-0.242	-0.008
2.326	0.204 K		0.331	-0.147	0.035
23	0.541 mK		0.301	0.306	-0.199
33	0.230 mK		0.294	0.331	-0.327
41	0.140 mK		0.291	0.341	-0.335
61	0.065 mK		0.286	0.361	0.003
94	0.053 mK		0.287	0.326	0.847

We begin by estimating the 11×11 matrix of second moments

$$\mathbf{C} \equiv \frac{1}{n_{\text{pix}}} \sum_{i=1}^{n_{\text{pix}}} \mathbf{y}_i \mathbf{y}_i^t \quad (7)$$

by averaging over all of the n_{pix} pixels i that were observed in all 11 frequencies (the sky region marked as “123456” in Figure 2)⁴. Therefore, the quantities

$$\sigma_j \equiv \mathbf{C}_{jj}^{1/2} \quad (8)$$

simply give the rms fluctuations at each frequency, and the correlation matrix

$$\mathbf{R}_{jk} \equiv \frac{\mathbf{C}_{jk}}{\sigma_j \sigma_k} \quad (9)$$

corresponds to the dimensionless correlation coefficients between all pairs of frequencies; $-1 \leq \mathbf{R}_{jk} \leq 1$ and $\mathbf{R}_{jj} = 1$. Defining the *normalized maps* \mathbf{z}_i as the input maps rescaled to have rms fluctuations of unity at each frequency, \mathbf{R} is simply the matrix of second moments of these normalized maps.

We then diagonalize the matrix \mathbf{R} , performing a standard eigenvalue decomposition

$$\mathbf{R} = \mathbf{P} \mathbf{\Lambda} \mathbf{P}^t, \quad (10)$$

where \mathbf{P} is an orthogonal matrix ($\mathbf{P}^t \mathbf{P} = \mathbf{P} \mathbf{P}^t = \mathbf{I}$) whose columns are the eigenvectors (principal components) and $\mathbf{\Lambda}_{jk} = \delta_{jk} \lambda_j$ is a diagonal matrix containing the corresponding eigenvalues, sorted in decreasing order. The eigenvalues λ_i are plotted in Figure 4, and the first three principal components are listed in Table 2 and shown in Figure 5. In this same table we also show the rms of the of each of the frequency maps calculated in the region 123456 (second column).

To help intuitively interpret this decomposition, Figure 6 shows maps of the first few principal components. Each principal component map a_i is defined as the dot product of the corresponding eigenvector with the normalized multi-frequency vector \mathbf{z}_i for each pixel. For each pixel i , we can therefore transform back and forth between the normalized multi-frequency vector \mathbf{z}_i and the principal component vector \mathbf{a} using the relations

⁴ If we had also removed the mean of each map in this region (an issue to which we return later), \mathbf{C} would simply be the covariance matrix between the 11 frequencies.

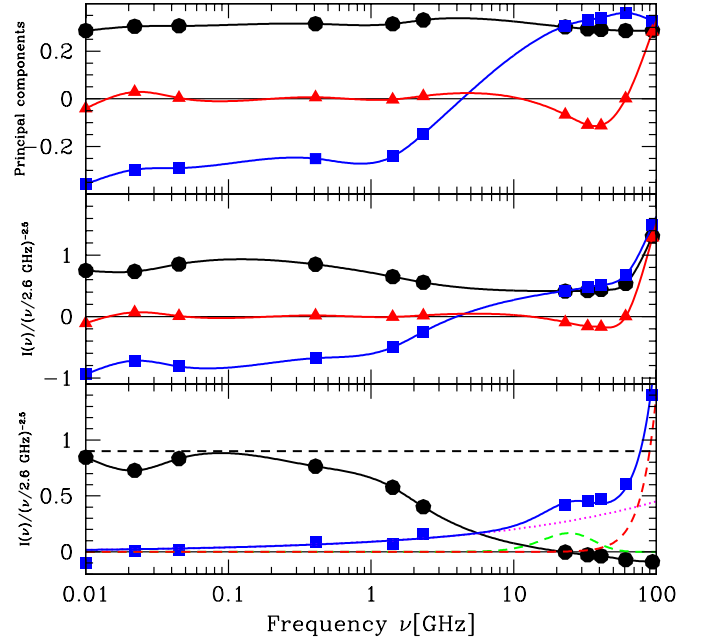


Figure 5. The frequency dependence is plotted for the first three principal components, labeled by black dots, blue squares and red triangles, respectively. The top panel is in units of the total rms fluctuations at each frequency, whereas the middle panel shows the sky brightness temperature divided by $(\nu/2.6 \text{ GHz})^{-2.5}$ to keep all frequencies on roughly the same scale. The bottom panel shows typical spectra of various physical components (8): synchrotron $\propto \nu^{-2.5}$ (long-dashed black), free-free $\propto \nu^{-2.15}$ (dotted magenta), spinning dust (long-dashed green) and thermal dust (long-dashed red). It also shows half the sum (black dots) and difference (blue squares) of the first two components, which are seen to behave roughly as synchrotron (with a spectral index that steepens toward higher frequency) and a sum of free-free, spinning and thermal dust (blue curve), respectively.

$$\mathbf{a}_i = \mathbf{P}^t \mathbf{z}_i, \quad \mathbf{z}_i = \mathbf{P} \mathbf{a}_i. \quad (11)$$

The principal component maps can be thought of as a division of the information in the 11 input maps into 11 mutually exclusive and collectively exhaustive chunks. They are mutually exclusive in the sense that they are uncorrelated:

$$\langle (\mathbf{P}^t \mathbf{z}) (\mathbf{P}^t \mathbf{z})^t \rangle = \mathbf{P}^t \langle \mathbf{z} \mathbf{z}^t \rangle \mathbf{P} = \mathbf{P}^t \mathbf{C} \mathbf{P} = \mathbf{\Lambda}. \quad (12)$$

They are collectively exhaustive in the sense that they together specify the multifrequency information completely through equation (11). Moreover, Figure 4 shows that almost all this information is contained in the first few principal components. Taking the trace of equation (10) shows that

$$\sum_{j=1}^{11} \lambda_j = \text{tr } \mathbf{\Lambda} = \text{tr } \mathbf{\Lambda} \mathbf{P}^t \mathbf{P} = \text{tr } \mathbf{P} \mathbf{\Lambda} \mathbf{P}^t = \text{tr } \mathbf{R} = 11, \quad (13)$$

since the diagonal elements of the correlation matrix are all unity. In other words, the total variance to be explained in the normalized multifrequency data is 11, with a contribution of unity from each of the 11 normalized input maps, and equation (12) shows that the j^{th} principal component map explains a variance λ_j , *i.e.*, a fraction $\lambda_j/11$ of the total.

Figure 4 shows that the first component (top panel of Figure 6) explains 80% of this total variance, the second component explains

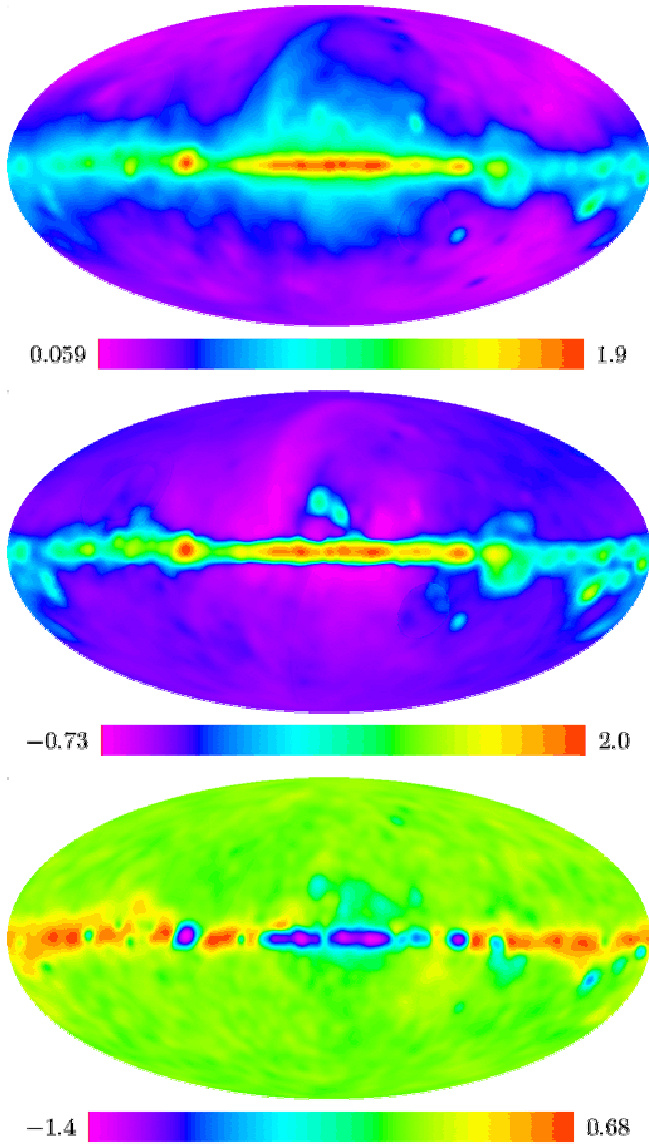


Figure 6. The first three principal components, which can be crudely interpreted as maps of total “stuff” (top), synchrotron fraction (middle) and thermal dust fraction of non-synchrotron emission (bottom). The color scale corresponds to $\lg(T/1\text{K})$ in the top panel, and $\sinh^{-1}(T/1\text{K})/\ln 10$ in the other panels to handle negative values (since $\sinh^{-1} x/\ln 10 \approx \lg|x|$ for $x \gg 1$ and for large positive and negative values, while it is roughly linear near zero).

another 19%, the third explains another 0.6%, and all the remaining eight components combined explain merely the last 0.3%. This is very convenient: we set out searching for a way to accurately parametrize the frequency dependence of the radio sky with as few parameters as possible, and have found that as few as two parameters capture more than 99% of the information.

Although principal component analysis is quite a standard data analysis technique (92), our analysis also includes some non-standard procedures, tailored for the particular challenges that our global sky modeling problem poses:

- We diagonalize \mathbf{R} rather than \mathbf{C} .
- We perform no mean removal.
- We make up for missing data by fitting to only the best principal components.

- We perform frequency interpolation by splining $\lg \sigma_i$ and the component spectra.

Let us now explain each of these procedures in more detail.

Diagonalizing \mathbf{R} rather than \mathbf{C} corresponds to using the normalized maps rather than the raw maps as input for the PCA. We made this choice because we are equally interested in providing a good fit (in terms of percent of rms explained) at all 11 frequencies. If one took the raw maps as input, the PCA would instead focus almost entirely on optimizing the fit to the lowest frequency maps, since the increase of synchrotron temperature towards lower frequencies causes them to have by far the largest rms signal measured in Kelvin. This usage of the normalized maps also has the advantage that the spectra of the dominant physical components become rather gently varying functions of frequency, which makes them much easier to linearly fit (see Figure 5). This eliminates the need for logarithmic fits and their above-mentioned problems.

In a standard PCA, one diagonalizes the covariance matrix $\langle(\mathbf{z} - \langle\mathbf{z}\rangle)(\mathbf{z} - \langle\mathbf{z}\rangle)^t\rangle$. We instead diagonalize the matrix $\langle\mathbf{z}\mathbf{z}^t\rangle$, *i.e.*, do not subtract off the mean from the normalized maps before computing their second moment matrix. This is because, as quantified in Section 4, this procedure makes the method more accurate in regions with incomplete data: whereas the principal components from the region with 11 frequency data work well across the entire sky (basically, because they reflect underlying physical emission mechanisms which are the same everywhere), the 11 mean values from this region are not at all representative for other regions, as they depend strongly on Galactic latitude. By not removing the mean, we also exploit the physical property that none of the dominant foreground components can ever contribute a negative intensity⁵.

Whereas a standard PCA can be performed in the region shown in Figure 2 where all 11 frequencies have been observed, we wish to build a global sky model covering the entire sky. Fortunately, we have $m_i \geq 6$ measured frequencies available everywhere, and have found that much fewer than 6 parameters are required for an excellent fit. We therefore take the best m_* principal components determined in the region with complete data and fit them to the data available. In Section 4 we will explore what is the best choice of m_* by quantifying the accuracy attained using $1 \leq m_* \leq 5$ components. We perform this fitting by modeling the observed data in a pixel with m_i observed frequencies as

$$\mathbf{z}_i = \tilde{\mathbf{P}}_i \tilde{\mathbf{a}}_i + \mathbf{n}_i, \quad (14)$$

where the tildes indicate that we are truncating to only m_* components: $\tilde{\mathbf{P}}_i$ is the $m_i \times m_*$ -dimensional matrix containing the m_* first principal components as its columns, $\tilde{\mathbf{a}}_i$ is the m_* -dimensional vector corresponding to the first m_* principal component maps (see Figure 5), \mathbf{z}_i contains the m_i normalized input maps that have data for this pixel, and the residual \mathbf{n}_i models random noise from both measurement errors and additional principal components not included in the fit. We perform this fitting separately for each pixel i by minimizing

$$\chi^2 \equiv (\mathbf{z}_i - \tilde{\mathbf{P}}_i \tilde{\mathbf{a}}_i)^t \mathbf{N}_i^{-1} (\mathbf{z}_i - \tilde{\mathbf{P}}_i \tilde{\mathbf{a}}_i), \quad (15)$$

which gives the solution

⁵ The only sky signal with a non-CMB spectrum that can give a negative temperature contribution is the thermal SZ effect, and it makes a rather negligible contribution compared to the synchrotron, free-free and dust components.

Table 3. Relative *rms* error in the sky region 123456.

ν [GHz]	Optimal	Principal components used					Unexplained fraction
		1	2	3	4	5	
0.010	0.062	0.543	0.078	0.072	0.065	0.066	0.00387
0.022	0.036	0.450	0.064	0.060	0.039	0.038	0.00126
0.045	0.035	0.438	0.046	0.046	0.038	0.038	0.00121
0.408	0.034	0.379	0.044	0.044	0.039	0.039	0.00115
1.420	0.111	0.386	0.135	0.135	0.150	0.196	0.01235
2.326	0.075	0.235	0.084	0.083	0.081	0.137	0.00562
23	0.015	0.463	0.058	0.026	0.026	0.026	0.00024
33	0.006	0.504	0.086	0.009	0.008	0.008	0.00004
41	0.009	0.519	0.089	0.017	0.015	0.015	0.00008
61	0.018	0.542	0.023	0.023	0.023	0.023	0.00033
94	0.057	0.538	0.225	0.059	0.059	0.059	0.00328

$$\tilde{\mathbf{a}}_i = [\tilde{\mathbf{P}}_i^t \mathbf{N}_i^{-1} \tilde{\mathbf{P}}_i]^{-1} \tilde{\mathbf{P}}_i^t \mathbf{N}_i^{-1} \mathbf{z}_i. \quad (16)$$

We describe our choice for the “noise” covariance matrix $\mathbf{N}_i \equiv \langle \mathbf{nn}^t \rangle$ in Section 4.

Let us summarize the above steps: we first find the principal components using the sky region with data at all 11 frequencies, then use the frequency dependence of these best m_* components to fit for maps of their amplitudes across the entire sky. This leaves us with an all-sky model predicting the emission at the 11 frequencies. However, we also wish to predict the emission at *any* frequency between 10 MHz $\leq \nu \leq$ 100 GHz. We do this by fitting the frequency dependence of both $\lg \sigma_j$ and each of the m_* principal components with a cubic spline as a function of $\lg \nu$. This works well only because, as seen in Figure 5, these are smooth, slowly varying functions. In contrast, it is notoriously difficult to perform useful interpolation of matrices, *e.g.*, \mathbf{R} , without wreaking havoc with their eigenvalues and physical behavior.

4 RESULTS

Above we have described how we construct our GSM. However, how accurate is it, and what does it teach us?

4.1 Accuracy of our GSM

4.1.1 Accuracy in the fully mapped region

Table 3 shows the accuracy of our GSM in the sky region where we have data at all 11 frequencies. As described in Section 3.1, we measure how accurately each map can be predicted by the other maps. Specifically, for each of the 11 frequencies, we compute the difference between this map and the map predicted by using only information from the other 10 maps, then tabulate the rms of this difference map divided by the rms of the observed map. Figure 7 illustrates this procedure for the more challenging all-sky case to which we return below: for these two example, the relative rms error is the rms of the bottom panel divided by the rms of the corresponding top panel.

Not surprisingly, Table 3 shows that using two components is much more accurate than using only one, reducing errors by almost an order of magnitude at some frequencies. Adding a third component is seen to further improve the accuracy, although not by as much, and mainly in the 20–40 GHz range. Adding a fourth component produces only minor gains, and reduces the 94 GHz accuracy

ever so slightly, and adding a fifth component makes the accuracy noticeably worse at three frequencies, suggesting that we are beginning to overfit the data just as with the above-mentioned cubic spline approach.

It is interesting to compare these accuracy numbers with what information theory tells us is the best possible case. The most accurate prediction for a given map using a linear combination of the others is easily computed using a standard linear regression analysis (92), and these optimal errors are listed in the second column of Table 3. A popular statistical measure of how useful something is for predicting something else is the fraction of the variance that it explains. Under the heading of “unexplained fraction”, we therefore also tabulate the fraction f_j of the map variance that is not explained by the other maps; this is simply the square of the rms residual, since the maps are normalized to have total variance of unity. Note that there is no need to actually perform a linear regression to compute these optimal numbers, as a simple derivation shows that they can be computed directly from the correlation matrix:

$$f_j = \frac{1}{(\mathbf{R}^{-1})_{jj} \mathbf{R}_{jj}}. \quad (17)$$

The results of this analysis are very encouraging. Table 3 shows that the residuals achieved by our GSM with three components are very close to these smallest possible ones, which means that we need not worry about having overlooked some alternative modeling method that does much better. The results also raise an important question: if linear regression is so good, why do we not use it instead of our GSM? The answer is that we cannot: regression only works when the matrix \mathbf{R} is known, and we can only compute \mathbf{R} when we already have data at the frequency that we are trying to model. In other words, whereas we can use regression for accuracy testing, where we already know the answer, it does not help us with modeling all the unobserved frequencies between 10 MHz to 100 GHz. We did explore the idea of predicting the \mathbf{R} -matrix entries corresponding to new frequencies using interpolation, but were unable to obtain useful results. In contrast, our GSM is straightforward to interpolate to other frequencies, because we simply need to interpolate the spectra plotted in Figure 5.

When we presented our GSM method described in Section 3, there were two details that we never specified: the choice of noise covariance matrix \mathbf{N} in equation (16) and the choice of m_* , the number of principal components to use. Let us now discuss these two choices in turn.

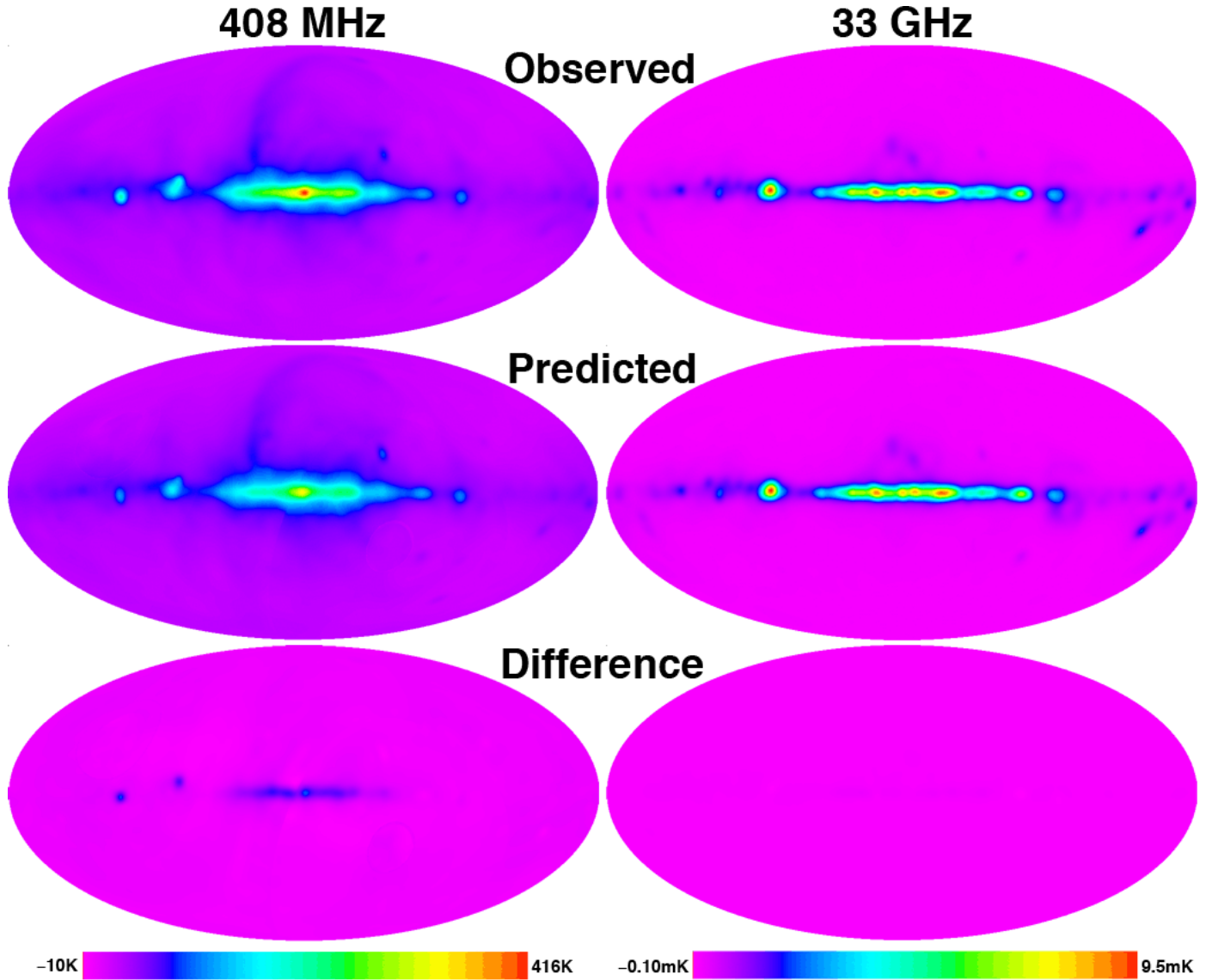


Figure 7. Accuracy of our model at 408 MHz (left column) and 33 GHz (right column). The top row shows the observed data (the Haslam and WMAP Ka-band maps), the middle row shows the maps predicted by our 3-component GSM without using the observed map above it, and the bottom row shows the observation minus the prediction (which is visually indistinguishable from zero for the 33 GHz case, because the residuals are less than 1% in and around the Galactic plane).

4.1.2 The noise covariance matrix

The “noise” is simply the residual signal in a map that we are unable to predict using the other maps, so it will contain contributions from both measurement errors in the input maps and sky emission mechanisms modeled with inadequate precision. Both of these contributions are captured by the remaining principal components not included in the fit, which according to equation (10) make a contribution to \mathbf{R} that is \mathbf{PAP}^t except with all eigenvalues from the included components set to zero. However, it is easy to show that adding noise for the included components has no effect on the solution of equation (16), so we get exactly the same result if we simply set $\mathbf{N} = \mathbf{PAP}^t = \mathbf{R}$. As a reality check, we also tried the alternative approach of setting \mathbf{N} equal to a diagonal matrix with the optimal variance values from Table 3 on the diagonal, and obtained very similar results.

4.1.3 Accuracy across the entire sky

How many principal components should we include to maximize the GSM accuracy? To determine this, we must quantify the accuracy not only in the best-case sky region where we have complete data, but also over the rest of the sky as well, since we ultimately care about the whole sky. Table 4 shows how this sky-averaged accuracy depends on the number of components used. Specifically, we have computed the relative rms error just as in Table 3, but separately for each of the 10 sky regions show in Figure 2, then computed their average weighting by sky area. The numbers show that the two best choices are 3 and 4 components. However, whereas these two choices were essentially tied in the fully observed region, $m_* = 3$ comes out slightly ahead in the all-sky average because it is twice as accurate at 1.42 GHz. This means that, although the 3-component model is slightly less sophisticated and therefore typically slightly less accurate, it is also more robust and less likely

Table 5. rms sky signal in K for regions of different cleanliness

ν [GHz]	region (←cleaner) (dirtier→)					
	1	2	3	4	5	6
0.010	203740	272337	304115	328310	281838	
0.022	27336	41972	63535	98153	118713	130600
0.045	5486	8347	13019	21285	31287	35926
0.408	20.0	30.0	52.0	103.3	182.9	230.4
1.420	0.744	1.021	1.614	3.016	5.356	6.839
2.326	0.150	0.238	0.487	1.184	2.196	2.760
23	0.000098	0.000260	0.001106	0.004140	0.010357	0.015078
33	0.000036	0.000097	0.000435	0.001693	0.004343	0.006444
41	0.000021	0.000056	0.000255	0.000996	0.002569	0.003851
61	0.000007	0.000024	0.000117	0.000433	0.001091	0.001639
94	0.000006	0.000022	0.000106	0.000332	0.000758	0.001078

Table 4. Relative error averaged over the entire sky

ν [GHz]	Principal components used				
	1	2	3	4	5
0.010	0.438	0.091	0.098	0.088	0.168
0.022	0.690	0.164	0.144	0.142	0.138
0.045	0.712	0.110	0.109	0.111	0.100
0.408	0.436	0.112	0.115	0.127	0.134
1.420	0.546	0.143	0.144	0.698	0.875
2.326	0.216	0.148	0.155	0.158	0.503
23	0.423	0.082	0.062	0.062	0.064
33	0.453	0.077	0.013	0.013	0.014
41	0.458	0.071	0.032	0.032	0.031
61	0.444	0.069	0.068	0.068	0.070
94	0.385	0.223	0.121	0.121	0.160

to go badly wrong in unusual parts of the sky. For this reason, we focus on the 3-component model in the rest of this paper.

Table 4 shows that the typical accuracy is around 10% for the frequencies below WMAP, and noticeably better for the four lowest WMAP-frequencies. It is striking that the 33 GHz accuracy is as good as 1.3%, which means that if WMAP had not made this particular map, as much as 99.97% of the sky variance at this frequency could have been predicted by the other maps (and this is not even counting the CMB signal, which we subtracted off at the outset). Also, as shown in the results for the WMAP 94 GHz map, the amount of noise in a map clearly worsens the accuracy to which we can reconstruct it.

4.1.4 Accuracy at different Galactic latitudes

It is difficult to quantify the accuracy of our GSM in a meaningful way with a single number, since the sky signal varies so dramatically with Galactic latitude: any measure of *absolute* error (in Kelvin) will therefore be dominated by the inner Galactic plane, while any measure of *relative* error will tend to be dominated by the cleanest regions where the signal-to-noise ratio is the poorest. To get a more nuanced picture of how accurate our GSM is, let us therefore quantify the relative errors separately for the regions shown in Figure 8, which subdivide the sky into six parts of increasing Galactic emission. They were defined in (18) by computing the four differences of WMAP maps at neighboring frequencies

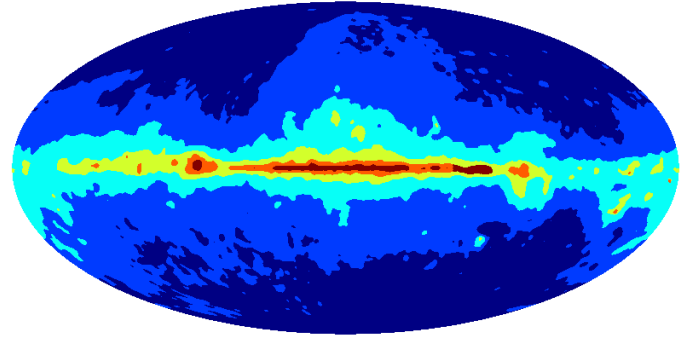


Figure 8. Our subdivision of the sky into six regions of decreasing cleanliness. From outside in, they correspond to WMAP-based junk map temperatures $T < 100\mu\text{K}$, $100\mu\text{K} - 300\mu\text{K}$, $300\mu\text{K} - 1\text{mK}$, $1\text{mK} - 3\text{mK}$, $3\text{mK} - 10\text{mK}$, and $T > 10\text{mK}$, respectively.

(to subtract out the CMB), computing the largest absolute value at each pixel, and making a contour plot of the resulting “junk map”. From outside in, the regions correspond to junk map temperatures $T < 100\mu\text{K}$, $100\mu\text{K} - 300\mu\text{K}$, $300\mu\text{K} - 1\text{mK}$, $1\text{mK} - 3\text{mK}$, $3\text{mK} - 10\text{mK}$, and $T > 10\text{mK}$, respectively, so the typical sky signal differs by about half an order of magnitude between neighboring regions. Table 5 shows that this scaling is roughly valid at all the WMAP frequencies, and that the differences between dirty and clean regions become less extreme towards lower frequencies. Although we of course do not have complete frequency coverage across the entire sky, comparing Figure 2 with Figure 8 shows that we are lucky to have coverage at all frequencies somewhere within each of the six sky regions of Figure 8, with the only exception that the very dirtiest region is not observed at 10 MHz.

Table 6 summarizes how the accuracy of our 3-component GSM depends on both frequency and Galactic signal level. At the sub-GHz frequencies relevant to 21cm tomography, we see that the accuracy is typically $\sim 10\%$ or better in the cleanest parts of the sky, and degrades in the inner Galactic plane. For the higher frequencies relevant to CMB research, the situation is the opposite: the accuracy is best in the dirtiest parts of the sky (as good as 1% at 33 and 41 GHz), but degrades in the cleanest regions. This is clearly due to the fact that detector noise is non-negligible at the higher WMAP frequencies, so that the lower the signal is, the lower the signal-to-noise level and the accuracy. Future WMAP data releases

Table 6. Relative error as a function of sky cleanliness

ν [GHz]	←cleaner region (dirtier→)					
	1	2	3	4	5	6
0.010	0.091	0.099	0.094	0.148	0.111	
0.022	0.080	0.082	0.136	0.210	0.306	0.451
0.045	0.094	0.102	0.095	0.108	0.158	0.202
0.408	0.084	0.088	0.072	0.125	0.170	0.190
1.420	0.187	0.133	0.144	0.180	0.157	0.129
2.326	0.147	0.160	0.158	0.165	0.170	0.167
23	0.111	0.070	0.083	0.073	0.062	0.050
33	0.062	0.022	0.013	0.012	0.011	0.011
41	0.091	0.052	0.042	0.039	0.034	0.028
61	0.270	0.067	0.071	0.082	0.079	0.067
94	0.766	0.164	0.095	0.124	0.136	0.135

are therefore likely to further improve the accuracy of our GSM at CMB frequencies.

Finally, it is important to remember that the errors in our downloadable GSM are likely to be even smaller than the tables above suggest, because a map used as “truth” in a test may itself have noise and systematic errors, and also because it uses all 11 input maps jointly, not merely 10 at a time. For example, one can clearly make vastly better predictions near 408 MHz than Table 6 suggests if the Haslam map is included in the modeling.

4.2 Implications for our input maps

An interesting byproduct of our modeling effort is an independent quality assessment of the 11 input maps. If two maps are highly correlated, this implies that none of them can be afflicted by large noise or systematic errors, which would have spoiled the correlation. More quantitatively, the unexplained variance fraction listed in Table 3 places an upper bound on the total contribution from detector noise and systematic errors in a map. If we focus on its square root, the optimal rms column in the same table, we see that the lowest frequency WMAP maps give the lowest residuals. This is not surprising, considering that in order to meet its CMB science goals, WMAP had to be designed with significantly stricter systematic error control than typical in radio astronomy. As mentioned above, the WMAP increase in residuals with frequency reflects the drop in foreground signal while detector noise remains important and roughly constant.

At the lower frequencies relevant to 21 cm tomography, we see that the 10–408 MHz map errors can be at most at the 10% level in the cleaner parts of the sky (see Table 6), and no more than 6% in the region where we have full frequency coverage (see Table 3, column 2). The remaining radio maps (at 1.42 GHz and 2.326 GHz) have error bounds about a factor two higher.

Finally, there is one kind of systematic error that our modeling cannot detect: an overall position-independent calibration error in a map. Because this would not affect the dimensionless correlation coefficients with other maps, it would not affect our goodness-of-fit either, merely cause corresponding calibration errors in the predictions.

4.3 Physical interpretation of our GSM

The goal of this paper is simply to model the Galactic emission, not to understand it physically. However, since our statistical results

automatically encode interesting physical information, let us briefly comment on possible interpretations.

4.3.1 Component interpretation

A number of physical components of Galactic emission in our frequency range have been thoroughly discussed in the literature, notably synchrotron radiation, free-free emission, spinning dust and thermal dust. However, we should not expect these physical components, which tend to be highly correlated, to match our principal components, which are by definition uncorrelated. We should instead expect our first principal component (top panel in Figure 6) to trace the total amount of “stuff”, and the remaining principal components to describe how the ratios of different physical components vary across the sky. The frequency dependence seen in Figure 5 confirms this. The first component is shown to contribute an essentially constant fraction of the rms at all frequencies, corresponding to $\lambda_1/11 \approx 80\%$ of the total variance.

The second component, which explains another $\lambda_2/11 \approx 19\%$ of the total variance, is seen to have the negative of a synchrotron-like spectrum below a few GHz, and a spectrum at higher frequencies that is suggestive of a sum of free-free emission, spinning dust and thermal dust. This suggests that this component encodes what fraction of the total emission is due to synchrotron radiation. Sure enough, the second panel in Figure 6 is seen to be negative in the north polar spur region which is known to be dominated by synchrotron emission, and positive in regions like the inner Galactic plane and the Large Magellanic Cloud where one expects higher fractions of non-synchrotron emission.

The third component, which explains two thirds of the remaining variance (and $\lambda_3/11 \approx 0.6\%$ of the total variance), is seen in Figure 5 to have a spectrum that looks like thermal dust at the high end, goes negative below that, and essentially vanishes below a few GHz where synchrotron radiation becomes dominant. This suggests crudely interpreting it as encoding what fraction of the non-synchrotron signal is due to thermal (vibrational) dust emission. It is unclear whether the 10 MHz blip in its spectrum is a fluke or reflects a physical correlation between dust properties and low-frequency synchrotron properties like self-absorption (93).

4.3.2 Synchrotron and non-synchrotron templates

As we discussed before, we do not expect our principal components to correspond directly to physical components, because the former are by definition uncorrelated while the latter are not (“stuff traces stuff”, and there tends to be more of everything at low Galactic latitudes). However, it is interesting to ask whether we can form linear combinations of our principal components that have a simple physical interpretation.

Interestingly, we can. In Figure 5, we see that taking the sum and difference of the first two principal components (from the second panel) gives components whose spectra look distinctly like what is theoretically expected for synchrotron and a combination of the other emission components, respectively (as seen in the bottom panel). First of all, Figure 5 (bottom) shows that the two new template spectra are approximately non-negative at all 11 frequencies. This is a non-trivial result, since generic 11-dimensional eigenvectors or combinations of them will have both significantly negative and significantly positive components — in contrast, we know that neither synchrotron, free-free nor dust emission can be negative. Second, the same figure shows that first template, which we will

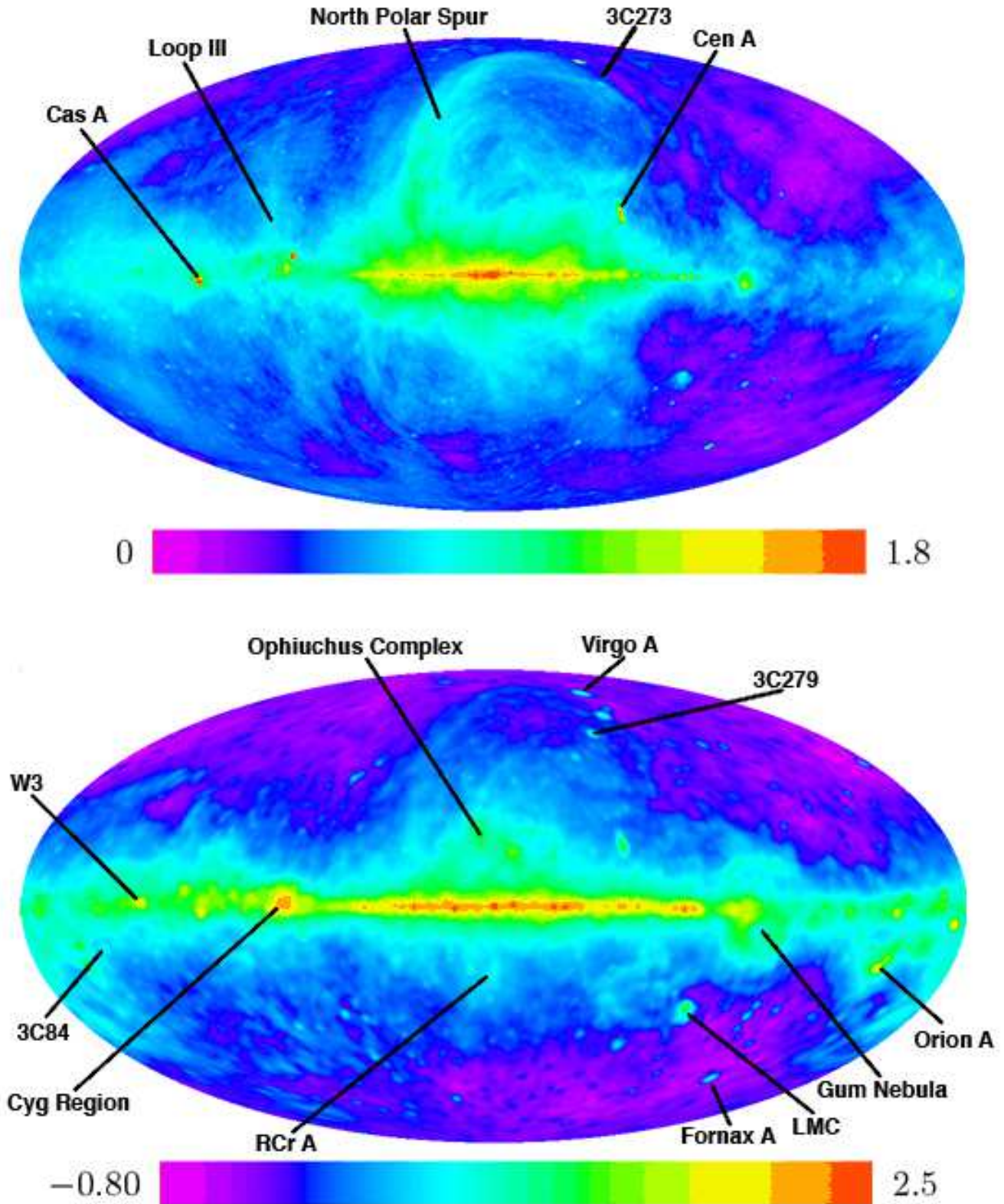


Figure 9. Our synchrotron (top) and non-synchrotron (bottom) templates are the sum and difference of our first two principal components, where the color scales corresponds to $\lg(T/1K)$. Labels indicate bright objects in our Galaxy such as supernova remnants (Cas A, North Polar Spur, Loop III), an emission nebula (Gum Nebula), giant molecular clouds (Orion A, R Corona Australis, the Ophiucus Complex, W3) and an active star-forming region (Cygnus Region) as well as bright extragalactic sources like giant elliptical galaxies (Virgo A, Fornax A), radio galaxies (Centaurus A, 3C84) and quasars (3C273, 3C279).

hereafter refer to as our synchrotron template, has a spectral index $\beta \approx -2.5$ at low frequencies, gradually steepening towards higher frequencies just as expected for synchrotron radiation (86; 87). In contrast, the second template, which we will refer to simply as our non-synchrotron template, is seen to have a spectrum such that $\nu^{2.5}I(\nu)$ rises toward higher frequencies, and can be fit by a sum of free-free, spinning dust (94) and thermal dust emission. The corresponding sky maps (the sums and differences of the first two principal components) are shown in Figure 9.

In other words, our spectral results are consistent with the interpretation that the top panel of Figure 9 is a diffuse synchrotron template while the bottom one is a template of diffuse non-synchrotron emission. As expected, known supernova remnants subtending large angles (Cas A, North Polar Spur and Loop III) are prominent in the synchrotron template, while diffuse dusty sources like the Cygnus Region stand out in the other template. However, we cannot make any such interpretations for the point sources that appear in the paper. This is because some point sources were removed from some of the low-frequency radio maps we used, which can fool our analysis into removing them from the synchrotron template. For example, in the 22 MHz map that we used, areas around the strong point sources Tau A, Cas A, Cyg A and Vir A. have been blanked. At 1420 MHz, only Cas A was blanked. Although it would be useful to repeat our analysis with new versions of the input maps where point sources have not been removed (or where they have been reinserted using measured fluxes), the present paper of course has the opposite focus: our key purpose is to model the diffuse emission for use in the *cleanest* parts of the sky, which are the ones most relevant to 21 cm tomography and CMB observations.

It is worth emphasizing the blind nature of our analysis: by simply forming those two unique linear combinations of our two dominant principal components for which the spectra were non-negative, our approach discovered the synchrotron and non-synchrotron spectra in the data using no physics input whatsoever.

4.4 Angular resolution options

To be able to use all 11 of our input maps, our spectral modeling has been performed at 5.1° , the lowest common denominator. If we make the approximation that the spectral shape, but not its amplitude, varies only slowly across the sky, then we can create a higher resolution global sky model by locking the amplitude to a higher resolution input map. For example, for each pixel, we can rescale all three principal components used by the same constant, chosen such that the prediction at 408 MHz matches the full resolution Haslam map. This procedure is illustrated in Figure 9: the top panel locks to the 1° Haslam map (recommended for applications below 1 GHz where synchrotron dominates) while the bottom panel locks to the WMAP 23 GHz map smoothed to 2° to suppress detector noise (recommended for applications at CMB frequencies). These 1° , 2° and 5.1° versions of our GSM are all available on the above-mentioned website. Figure 10 shows examples of our output maps at 5.1° resolution.

5 CONCLUSIONS

We have presented a global sky model for 10 MHz to 100 GHz Galactic emission derived from all publicly available total power large-area radio surveys, digitized with optical character recognition when necessary and compiled into a uniform format. Both

our data compilation and software for returning a predicted all-sky map at any frequency from 10 MHz to 100 GHz are available at <http://space.mit.edu/home/angelica/gsm>.

We found that a PCA-based model with only three components can fit the 11 most accurate data sets (at 10, 22, 45 & 408 MHz and 1.42, 2.326, 23, 33, 41, 61, 94 GHz) to an accuracy around 1%-10% depending on frequency and sky region. We found that using these three principal components comes very close to the maximal accuracy allowed by information theory, with the added advantage of allowing robust frequency interpolation and some physical interpretation. The fact that our model has so few fitting parameters in a given spatial direction also makes it rather robust to the input data: a map with lots of noise or systematic errors will have smaller correlations with other maps, and therefore and get “voted down” by the other maps and given less weight.

Strong correlations between different physical emission mechanisms would explain why such accurate fits are possible with fewer principal components than known physical components: one rapidly counts beyond three when including free-free emission, spatial variations of the synchrotron and dust spectra, etc.

We have focused entirely on unpolarized Galactic emission. To help maximize the future scientific impact of 21 cm tomography experiments, it will be important to extend this work to both extragalactic point sources and polarized emission. Since these experiments will provide a gold mine of cosmological information buried by under $\sim 10^4$ times larger foreground signals, this should be well worth the effort!

ACKNOWLEDGEMENTS

We would like to thank Ben Gold, Jacqueline Hewitt, Miguel Morales, Wolfgang Reich and Matias Zaldarriaga for helpful comments, and Hector Alvarez and Koitiro Maeda for generously allowing us to use the 45 MHz radio survey. We thank the the WMAP team for making their data public via the Legacy Archive for Microwave Background Data Analysis (LAMBDA) at <http://lambda.gsfc.nasa.gov>. Support for LAMBDA is provided by the NASA Office of Space Science. We thank Krzysztof Górski and collaborators for creating the HEALPix package (83). This work was supported by NSF grants AST-0607597, 0134999 and 6915954, by NASA grant NAG5-11099, by the Kavli Foundation, by the fellowships from the David and Lucile Packard Foundation and the Research Corporation, and support from the Australian Research Council through Federation Fellowship FF0561298.

REFERENCES

- (1) “A method for subtracting foregrounds from multifrequency CMB sky maps”, M Tegmark, G Efstathiou 1996, *MNRAS*, **281**, 1297
- (2) “Simulations of the Microwave Sky and of its Observations”, F R Bouchet, R Gispert, N Aghanim, J R Bond, A De Luca, E Hivon, B Maffei 1995, *Space Science Rev.*, **74**, 37
- (3) “The mm/sub-mm foregrounds and future CMB space missions”, F R Bouchet, R Gispert, J L Puget 1996, proc. in *Unveiling the Cosmic Infrared Background*, E Dwek (Ed), Baltimore, Maryland USA, Editions AIP, p. 255
- (4) “Removing Real-World Foregrounds from Cosmic Microwave Background Maps”, M Tegmark 1998, *ApJ*, **502**, 1

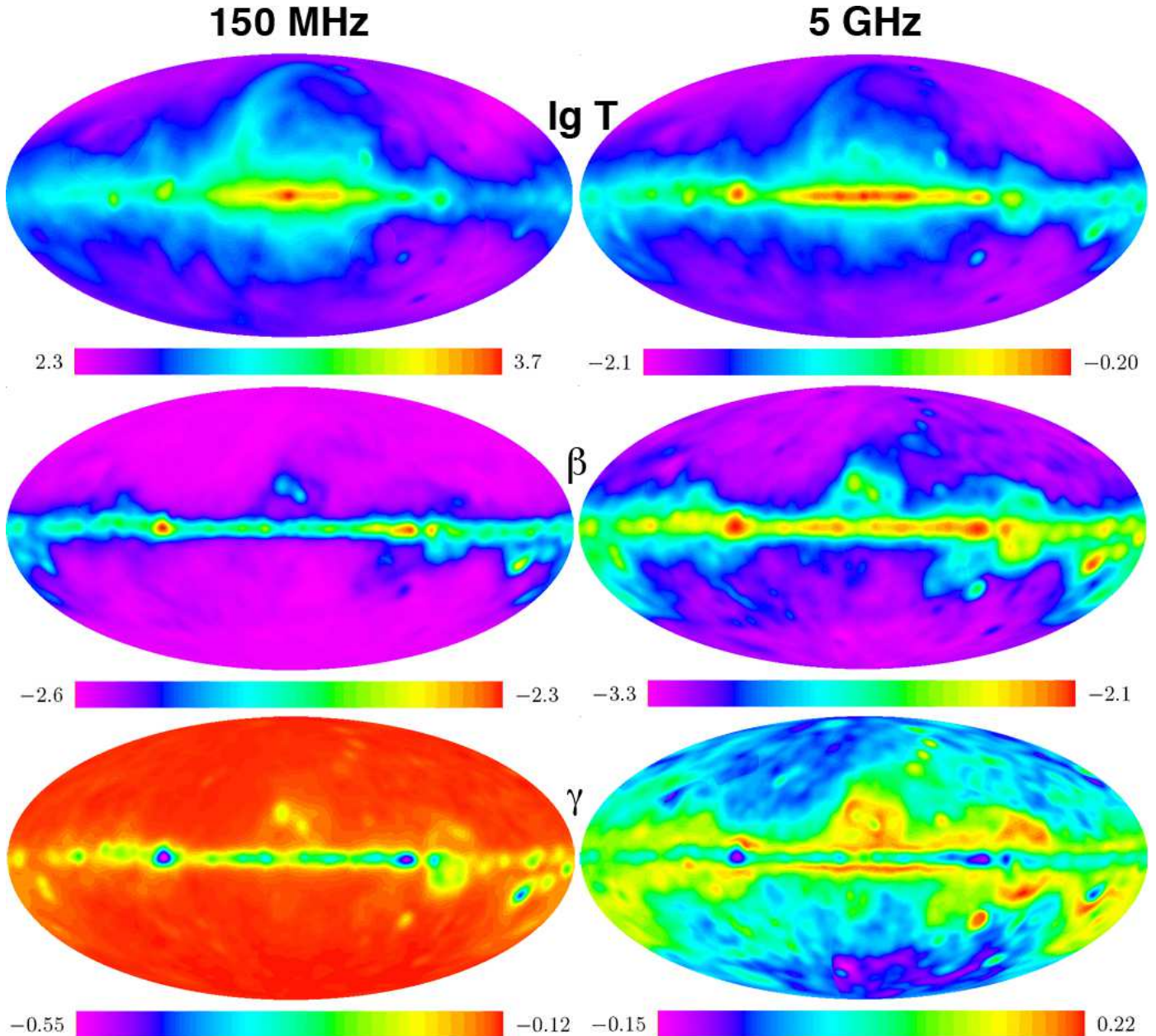


Figure 10. Sky maps (from top to bottom) of the temperature, spectral index β , and “the running” (or variation) of spectral index γ at 150 MHz (shown on the left) and 5 GHz (shown on the right). Whereas the 150 MHz emission is dominated by synchrotron radiation with a spectrum that is both falling ($\beta \sim -2.5$) and steepening ($\gamma < 0$), the 5 GHz emission has a much broader range of spectral indices that are mostly getting less negative towards higher frequency ($\gamma > 0$).

- (5) “Microwave Foregrounds”, A de Oliveira-Costa, M Tegmark (Ed.) 1999, ASP Conf.Ser. (San Francisco: ASP)
- (6) “Multi-frequency wiener filtering of CMB data with polarization”, F R Bouchet, S Prunet, S K Sethi 1999, *MNRAS*, **302**, 663
- (7) “Foregrounds and CMB experiments I. Semi-analytical estimates of contamination”, F R Bouchet, R Gispert 1999, *NewA*, **4**, 443
- (8) “Foregrounds and forecasts for the cosmic microwave background”, M Tegmark, D J Eisenstein, W Hu, A de Oliveira-Costa 2000, *ApJ*, **530**, 133-165
- (9) “The angular power spectra of polarized Galactic synchrotron”, M Tucci, E Carretti, S Cecchini, R Fabbri, M Orsini, E Pierpaoli E, 2000, *NewA*, **5**:181
- (10) “Power spectrum of the polarized diffuse Galactic radio emission”, C Baccigalupi, C Burigana, F Perrotta, G De Zotti, L La Porta, D Maino, M Maris, R Paladini 2001, *A&A*, **372**, 8
- (11) “A New Spin on Galactic Dust”, A de Oliveira-Costa, M Tegmark, D P Finkbeiner, R D Davies, C M. Gutierrez, L M Haffner, A W Jones, A N Lasenby, R Rebolo, R J Reynolds, S L Tufte, R A Watson 2002, *ApJ*, **567**, 363
- (12) “The power-law behaviors of angular spectra of polarized Galactic synchrotron”, M Bruscoli, M Tucci, V Natale, E Carretti, R Fabbri, C Sbarra, S Cortiglioni 2002, *NewA*, **7**, 171
- (13) “Polarization angular spectra of Galactic synchrotron emis-

- sion on arcminute scales”, M Tucci, E Carretti, S Cecchini, L Nicastro, R Fabbri, B M Gaensler, J M Dickey, N M McClure-Griffiths 2002, *ApJ*, **579**, 607
- (14) “Towards a model of full-sky Galactic synchrotron intensity and linear polarization: A re-analysis of the Parkes data”, G Giardino, A J Banday, K M Górski, K Bennett, J Jonas, J Tauber 2002, *A&A*, **387**, 82
- (15) “The large-scale polarization of the microwave background and foreground”, A de Oliveira-Costa, M Tegmark, C O’Dell, B Keating, P Timbie, G Efstathiou, G Smoot 2003, *Phys. Rev. D*, **68**, 083003
- (16) “First Year Wilkinson Microwave Anisotropy Probe (WMAP) Observations: Foreground Emission”, C Bennett, R S Hill, G Hinshaw, M R Nolta, N Odegard, L Page, D N Spergel, J L Weiland, E L Wright, M Halpern, N Jarosik, A Kogut, M Limon, S S Meyer, G S Tucker, E Wollack 2003, *ApJS*, **148**, 97
- (17) “The Quest for Microwave Foreground X”, A de Oliveira-Costa, M Tegmark, C M Gutierrez, A W Jones, R D Davies, A N Lasenby, R Rebolo, R A Watson 2004, *ApJL*, **606**, L89
- (18) “A high resolution foreground cleaned CMB map from WMAP”, M Tegmark, A de Oliveira-Costa, A Hamilton 2003, *Phys. Rev. D*, **68**, 123523
- (19) “The significance of the largest scale CMB fluctuations in WMAP”, A de Oliveira-Costa, M Tegmark, M Zaldarriaga, A Hamilton 2004, *Phys. Rev. D*, **69**, 063516
- (20) “A multifrequency angular power spectrum analysis of the Leiden polarization surveys”, L La Porta, C Burigana 2006, *A&A*, **457**, 1L
- (21) “Three Year Wilkinson Microwave Anisotropy Probe (WMAP) Observations: Temperature Analysis”, G Hinshaw, M R Nolta, C Bennett, R Bean, O Dore, M R Greason, M Halpern, R S Hill, N Jarosik, A Kogut, E Komatsu, M Limon, N Odegard, S S Meyer, L Page, H V Peiris, D N Spergel, G S Tucker, L Verde, J L Weiland, E Wollack, E L Wright 2007, *ApJS*, **170**, 288
- (22) “CMB Multipole Measurements in the Presence of Foregrounds”, de Oliveira-Costa, Tegmark 2006, *Phys. Rev. D*, **74**, 023005
- (23) “CMB anisotropy power spectrum using linear combinations of WMAP maps”, R Saha, S Prunet, P Jain, T Souradeep 2007, astro-ph/07063567
- (24) “A Method for Separating the Physics from the Astrophysics of High-Redshift 21cm Fluctuations”, R Barkana, A Loeb 2005, *ApJ*, **624**, 65
- (25) “Detecting the Earliest Galaxies Through Two New Sources of 21cm Fluctuations”, R Barkana, A Loeb 2005, *ApJ*, **626**, 1
- (26) “Probing the Epoch of Early Baryonic Infall Through 21cm Fluctuations”, R Barkana, A Loeb 2005, *MNRAS*, **363**, 36
- (27) “Separating out the Alcock-Paczynski Effect on 21cm Fluctuations”, R Barkana 2006, *MNRAS*, **372**, 259
- (28) “The Physics and Early History of the Intergalactic Medium”, R Barkana, A Loeb 2007, *Rep. Prog. Phys.*, **70**, 627
- (29) “First Light”, A Loeb 2006, astro-ph/0603360
- (30) “21cm Cosmology”, A Loeb 2006, *Sci. Am*, **11**, 46
- (31) “The 21 cm Forest: Radio Absorption Spectra as Probes of Minihalos Before Reionization”, S Furlanetto, A Loeb 2002, *ApJ*, **579**, 1
- (32) “Statistical Probes of Reionization With 21 cm Tomography”, S Furlanetto, M Zaldarriaga, L Hernquist 2004, *ApJ*, **613**, 16
- (33) “21 Centimeter Fluctuations from Cosmic Gas at High Redshifts”, M Zaldarriaga, S Furlanetto, L Hernquist 2004, *ApJ*, **608**, 622
- (34) “Observing the Reionization Epoch Through 21 Centimeter Radiation”, S Furlanetto, A Sokasian, L Hernquist 2004, *MNRAS*, **347**, 187
- (35) “LOFAR: A new radio telescope for low frequency radio observations: Science and project status”, H Rottgering, A G de Bruyn, R P Fender, J Kuijpers, M P van Haarlem, M Johnston-Hollitt, G K Miley 2003, *Tsra.Symp.*, **21**, 69
- (36) “LOFAR, a new low frequency radio telescope”, H Rottgering 2003, *NewAR*, **47**, 405
- (37) “LOFAR as a Probe of the Sources of Cosmological Reionisation”, S Zaroubi, J Silk 2005, *MNRAS*, **360**, 64
- (38) “Probing the Dark Ages with the Square Kilometer Array”, C Carilli, S Furlanetto, F Briggs, M Jarvis, S Rawlings, H Falcke 2004, *NewAR*, **48**, 1029
- (39) “Observations of HI 21cm absorption by the neutral IGM during the epoch of re-ionization with the Square Kilometer Array”, C Carilli, N Gnedin, S Furlanetto, F Owen 2004, *NewAR*, **48**, 1053
- (40) “Searching for Early Ionization with the Primeval Structure Telescope”, J Peterson, U Pen, X Wu X 2006, *IAUJD*, **12**, 18
- (41) “Polarization of 21cm Radiation from the Epoch of Reionization”, D Babich, A Loeb 2005, *ApJ*, **635**, 1
- (42) “Power Spectrum Sensitivity and the Design of Epoch of Reionization Observatories”, M F Morales 2005, *ApJ*, **619**, 678
- (43) “21 cm Tomography of the High-Redshift Universe with the Square Kilometer Array”, S Furlanetto, F Briggs 2004, *NewAR*, **48**, 1039
- (44) “Polarization Signals of the 21 cm Background from the Era of Reionization”, A Cooray, S Furlanetto 2005, *MNRAS*, **359**, 47
- (45) “Toward Epoch of Reionization Measurements with Wide-Field Radio Observations”, M F Morales, J N Hewitt 2004, *ApJ*, **615**, 7
- (46) “Twenty-one Centimeter Tomography with Foregrounds”, X Wang, M Tegmark, M Santos, L Knox 2006, *ApJ*, **650**, 529
- (47) “The Sensitivity of First Generation Epoch of Reionization Observatories and Their Potential for Differentiating Theoretical Power Spectra”, J D Bowman, M F Morales, J N Hewitt 2006, *ApJ*, **638**, 20
- (48) “Improving Foreground Subtraction in Statistical Observations of 21 cm Emission from the Epoch of Reionization”, M F Morales, J D Bowman, J N Hewitt 2006, *ApJ*, **648**, 767
- (49) “Cosmology at Low Frequencies: The 21 cm Transition and the High-Redshift Universe”, S Furlanetto, S P Oh, F Briggs 2006, *Phys.Rept.*, **433**, 181-301
- (50) “A 408 MHz all-sky continuum survey. II - The atlas of contour maps”, C G T Haslam, C J Salter, H Stoffel, W E Wilson 1982, *A&AS*, **47**, 1
- (51) “Survey of the galactic background radiation at 3.93 and 6.55 MHz”, J K Alexander, J C Novaco 1974, *Astron. J*, **79**, 777
- (52) “A map of the northern sky at 10 MHz”, J L Caswell 1976, *MNRAS*, **177**, 601
- (53) “A 10 MHz Map of the Galaxy”, H V Cane, W C Erickson 2001, *Radio Science*, **36**, 1765
- (54) “Observations of the southern sky at 10.02 MHz”, P A Hamilton, R F Haynes 1968, *AuJPh*, **21**, 895
- (55) “The spectrum of the radio background between 13 and 404 MHz”, A H Bridle 1967, *MNRAS*, **136**, 219
- (56) “Galactic radio emission below 16.5 MHz and the galactic emission measure”, G R A Ellis 1982, *AuJPh*, **35**, 91

- (57) “The radio emission from the Galaxy at 22 MHz”, R S Roger, C H Costain, T L Landecker, C M Swerdlyk 1999, *A&AS*, **137**, 7
- (58) “The spectrum of the galactic radio emission: I. Observations of low resolving power”, A J Turtle, J F Pugh, S Kenderdine, I I K Pauliny-Toth 1962, *MNRAS*, **124**, 297
- (59) “A survey of the southern sky at 30 Mc/s”, D S Mathewson, N W Broten, D J Cole 1965, *AuJPh*, **18**, 665
- (60) “A 30 MHz map of the whole sky”, H V Cane 1978, *AuJPh*, **31**, 561
- (61) “A synthesis map of the sky at 34.5 MHz”, K S Dwarakanath, N Udaya Shankar 1990, *JApA*, **11**, 323
- (62) “A survey of the radio background at 38 MHz”, J Milogradov-Turin, F G Smith 1973, *MNRAS*, **161**, 269
- (63) “A 45-MHz continuum survey of the southern hemisphere”, H Alvarez, J Aparici, J May, F Olmos 1997, *A&AS*, **124**, 205
- (64) “A 45-MHz continuum survey of the northern hemisphere”, K Maeda, H Alvarez, J Aparici, J May, P Reich 1999, *A&AS*, **140**, 145
- (65) “The Galactic Metre Wave Radiation: A two-frequency survey between declinations $+25^\circ$ and -25° and the preparation of a map of the whole sky”, T L Landecker, R Wielebinski 1970, *AJPAS*, **16**, 1
- (66) “Galactic Radiation at Radio Frequencies. I. 100 Mc/s. Survey”, J G Bolton, K C Westfold 1950, *AuJPh*, **3**, 19
- (67) “A survey of the southern sky at 153 MHz”, P A Hamilton, R F Haynes 1969, *AuJPh*, **22**, 839
- (68) “Cosmic Static”, G Reber 1944, *Ap. J.*, **100**, 279
- (69) “A survey of galactic radiation at 178 Mc/s”, A J Turtle, J E Baldwin 1962, *MNRAS*, **124**, 459
- (70) “Survey of Galactic Radio-Noise at 200 Mc/s”, C W Allen, C S Gum 1950, *AuJPh*, **3**, 224
- (71) “Durchmusterung der allgemeinen Radiofrequenz-Strahlung bei 200 MHz. Mit 8 Textabbildungen”, F Dröge, W Priester 1956, *Zeitschrift für Astrophysik*, **40**, 236
- (72) “A survey of the background radiation at a frequency of 404 Mc/s, I”, I K Pauliny-Toth, J R Shakeshaft 1962, *MNRAS*, **124**, 61
- (73) “A survey of the continuum radiation at 820 MHz between declinations -7 and $+85$. I. Observations and reductions”, E M Berkhuijsen 1972, *A&AS*, **5**, 263
- (74) “A radio continuum survey of the northern sky at 1420 MHz. I”, W Reich 1982, *A&AS*, **48**, 219
- (75) “A radio continuum survey of the northern sky at 1420 MHz. II”, P Reich, W Reich 1986, *A&AS*, **63**, 205
- (76) “A radio continuum survey of the southern sky at 1420 MHz. The atlas of contour maps”, P Reich, J C Testori, W Reich 2001, *A&A*, **376**, 861
- (77) “The 2.3 GHz continuum survey of the GEM project”, C Tello, T Villela, S Torres, M Bersanelli, G F Smoot, I S Ferreira, A Cingo, J Lamb, D Barbosa, D Perez-Becker, S Ricciardi, J A Curriuan, P Platania, D Maino 2007, astro-ph/07123141
- (78) “The Rhodes/HartRAO 2326-MHz radio continuum survey”, J L Jonas, E E Baart, G D Nicolson 1998, *MNRAS*, **297**, 977
- (79) <http://space.mit.edu/home/angelica/gsm>
- (80) “A sky temperature survey at 19.2 GHz using a balloon borne Dicke radiometer for anisotropy tests of the cosmic microwave background”, D A Cottingham 1987, Ph.D. Thesis Princeton Univ., NJ
- (81) “Limits of Gaussian fluctuations in the cosmic microwave background at 19.2 GHz”, S P Boughn, E S Cheng, D A Cottingham, D J Fixsen 1992, *ApJ*, **391**, 49
- (82) “Four-Year COBE DMR Cosmic Microwave Background Observations: Maps and Basic Results”, C L Bennett, A J Banday, K M Górski, G Hinshaw, P Jackson, P Keegstra, A Kogut, G F Smoot, D T Wilkinson, E L Wright 1996, *ApJ*, **464**, 1
- (83) “HEALPix: A Framework for High-Resolution Discretization and Fast Analysis of Data Distributed on the Sphere”, K M Górski, E Hivon, A J Banday, B D Wandelt, F K Hansen, M Reinecke, M Bartelmann 2005, *ApJ*, **622**, 759
- (84) “Five-Year Wilkinson Microwave Anisotropy Probe (WMAP) Observations: Data Processing, Sky Maps, and Basic Results”, G Hinshaw, J L Weiland, R S Hill, N Odegard, D Larson, C L Bennett, J Dunkley, B Gold, M R Greason, N Jarosik, E Komatsu, M R Nolte, L Page, D N Spergel, E Wollack, M Halpern, A Kogut, M Limon, S S Meyer, G S Tucker, E L Wright 2008, astro-ph/0803.0732
- (85) “Radiative Processes in Astrophysics”, G B Rybicki, A P Lightman 1979, p.167-194
- (86) “Galactic dust emission and the cosmic microwave background”, A J Banday, A W Wolfendale 1991, *MNRAS*, **248**, 705
- (87) “The 2326 MHz radio continuum emission of the Milky Way”, J Jonas 1999, Ph.D. Thesis, Rhodes University (South Africa)
- (88) “The Shape of Radio Spectra of Spurs Between 38, 408 and 1420 MHz”, J Milogradov-Turin, S Nikolic 1995, *BABel*, **152**, 11
- (89) “Spectral index variations of the Galactic radio continuum emission - Evidence for a Galactic wind”, P Reich, W Reich 1988, *A&A*, **196**, 211
- (90) “A map of spectral indices of the Galactic radio continuum emission between 408 MHz and 1420 MHz for the entire northern sky”, P Reich, W Reich 1988, *A&AS*, **74**, 7
- (91) “A Determination of the Spectral Index of Galactic Synchrotron Emission in the 1-10 GHz Range”, P Platania, M Bensadoun, M Bersanelli, G de Amici, A Kogut, S Levin, D Maino, G F Smoot 1998, *ApJ*, **505**, 473
- (92) “Numerical Recipes”, W H Press, S A Teukolsky, W T Vetterling, B P Flannery 1992, Cambridge University Press, p. 931
- (93) “Interstellar Absorption of the Galactic Polar Low-Frequency Radio Background Synchrotron Spectrum as an Indicator of Clumpiness in the Warm Ionized Medium”, J D Peterson, W R Webber 2002, *ApJ*, **575**, 217
- (94) “Magnetic Dipole Microwave Emission from Dust Grains”, B Draine, A Lazarian 1998, *ApJ*, **494**, L19